Advanced Steel Construction – Vol. 21 No. 2 (2025) 136–146
DOI:10.18057/IJASC.2025.21.2.5

NONLINEAR ANALYSIS OF REINFORCED BEAM-COLUMN JOINTS WITH HIGH STRENGTH STEEL SINGLE-RIBBED PLATES

Xiu-Yuan Fang [1], Ze-Qing Wan[1, 2, *], Hong-Wei Ma [1, 2] and Yu Zhang [1]

[1] *College of Civil Science and Engineering, Yangzhou University, Yangzhou 225127, China*
[2] *State Key Laboratory of Green Building in Western China, Xi'an University of Architecture & Technology, Xi'an 710055, China*
* *(Corresponding author: E-mail: zqwan@yzu.edu.cn)*

ABSTRACT

In recent years, with the continuous development and wide application of high-strength steel in the field of construction, the research on the performance optimization of beam-column joints in high-strength steel structures has become increasingly important. This study aims to investigate the hysteretic performance of high-strength steel single-ribbed reinforced beam-column joints. Based on high strength steel properties test and tensile test of welded joint plate, two reference groups are established: high-strength steel common beam-column joints and ordinary steel single-ribbed reinforced beam-column joints. Finite element models are developed for the three types of joints to analyze their stress patterns, failure modes, hysteretic curves, skeleton curves, ductility, ultimate bearing capacity, and energy dissipation capacity under low cyclic reciprocating loads. It is found that high-strength steel single-rib reinforced beam-column joints can enhance the deformation capacity and initial stiffness of the joints. They exhibit improved ductility and energy dissipation capacity, as well as increased joint stiffness and a slower rate of stiffness degradation. This study provides valuable data for the design methods of high-strength steel structure beam-column joints.

ARTICLE HISTORY

Received: 6 June 2024
Revised: 23 December 2024
Accepted: 1 January 2025

KEYWORDS

High-strength steel;
Single ribbed plate reinforced type;
Beam-column joints;
Finite element;
Nonlinear analysis

1. Introduction

Driven by the demand of supply-side structural reform, the conditions for the application and development of high-performance steel structures are becoming increasingly mature. High-strength steel structures can reduce component sizes and significantly decrease material volume and weight, offering substantial social and economic benefits [1-2]. However, with the enhancement of strength, plasticity, toughness, and ductility are reduced, making welding high-strength steel challenging and becomes the main factor affecting the fatigue life of components [3], thereby limiting the widespread adoption of high-strength steel. Simultaneously, traditional steel frame beam-column joints are susceptible to brittle fracture, with most damage occurring at the flanges. An effective approach to address this issue is by eliminating the plastic hinge formation at the beam-column flange contact surface [4]. Currently, commonly used improved nodes include weakened nodes and strengthened nodes. Weakened nodes achieve outward plastic hinge formation by reducing the beam's bearing capacity [5], while strengthened nodes force the plastic hinge to occur far from the beam-column butt weld by reinforcing the beam end section [6]. The single-ribbed stiffened joint falls under the category of ribbed stiffened joints and exhibits excellent plastic deformation capacity and energy dissipation capacity.

Currently, many scholars both domestically and internationally have conducted relevant research on high-strength steel single-rib reinforced joints. Zong Liang et al. [7] conducted experiments and numerical simulations on Q690D high-strength steel butt welds, obtaining mechanical properties and fatigue performance and verifying the validity of the numerical simulation method for fatigue assessment. Liu et al. [8] studied the influence of optimized welding parameters on the structural distortion of S690 high strength steel thin-plate. Jordao et al. [9] conducted finite element numerical analysis on beam-column joints composed of S355 ordinary steel and S690 high-strength steel, calibrating it with full-scale model test results. Guo et al. [10] designed a kind of high-strength steel bending beam-column joint connected by angle steel. Through static loading test and finite element analysis, it was verified that this kind of reinforced joint can significantly improve the bearing capacity of the joint.. Hongchao G et al. [11] performed low-cyclic loading tests on six Q690 high-strength steel plate reinforced joints, demonstrating higher bearing capacity of the high-strength steel plate, and a combination of Q690 and ordinary steel yielded higher ductility. Lu et al. [12] made a nonlinear analysis of a beam-end ribs reinforced joint, and the results showed that the joint could make the plastic hinge move outward effectively. Wang et al. [13] analyzed the parameters of reinforced joints with single rib, and gave the design method of reinforced joints with single rib. Yang Tao et al. [14] carried out ANSYS finite element analysis on the mechanical properties of the joint domain with stiffened ribs.

Presently, there exists a plethora of research achievements on the mechanical properties of high-strength steel, yet there is a gap in the investigation of welded joint properties, primarily conducted through experimental methods. The finite element method, used as an auxiliary check calculation, simplifies the setup of its simulated contact.

In this study, the validity of the finite element simulation method is verified by the comparison of uniaxial tensile tests of high strength steel welded joint plates. To provide design data for high-strength steel structure beam-column joints, three sets of beam-column joints were established using ABAQUS software to analyze their hysteretic performance, and further optimization of single-rib joint parameters was conducted.

2. Material test and welded joint plate test

2.1. Q690D high strength steel properties test

In this test, the performance test of Q690D high-strength steel was conducted using the UTM5305 electronic universal testing machine, which has a maximum measuring range of 30 tons. For strain measurement, the YSJ50/10-ZC electronic extensometer with a measuring range of 2mm to 50mm was used. The material property test results serve as the basis for material property parameters used in test data analysis, finite element numerical simulation, and theoretical calculations.

Fig. 1 UTM5305 electronic universal testing machine

Following the guidelines outlined in "Steel and Steel Products - Mechanical Properties Test Sampling Location and Sample Preparation" (GB/T2975-2018) [15], samples were extracted from the same batch of high-strength steel welded joint plate specimens. The samples were then prepared with thicknesses of 6mm, 8mm, 10mm, and 16mm, respectively. The property test for Q690D high-strength steel was conducted in the Structure Laboratory of Yangzhou University, specifically through a unidirectional tensile test. Prior to stretching the specimen, suitable fixtures were chosen based on the plate thickness, and the specimen was positioned vertically at the center. The loading device setup is depicted in Fig.1.

Given that Q690D high-strength steel exhibits no distinct yield platform and directly enters nonlinear strengthening after yield, the nominal stress corresponding to 0.2% strain is considered as the yield strength and denoted as $f_{0.2}$. The results of material properties test for each group are shown in Table 1. The average value in this test is 234.7GPa, providing essential material constitutive parameters for subsequent finite element analysis.

Table 1
Test results of Q690D high strength steel properties

Specimen thickness	The sample number	Sectional area	Modulus of elasticity	Yield strength	Tensile strength	Elongation
		A/mm^2	E/GPa	$f_{0.2}$/MPa	f_u/MPa	ε/%
6mm	6-1	89.82	223.6	712.12	792.53	23.44
	6-2	88.77	242.2	713.53	795.14	19.46
	6-3	89.43	229.4	714.64	796.42	19.62
8mm	8-1	116.74	237.4	710.27	789.63	18.50
	8-2	119.84	236.8	708.74	789.55	18.28
	8-3	117.74	238.0	710.65	787.64	18.37
10mm	10-1	148.63	223.7	713.17	793.44	21.84
	10-2	148.20	229.8	712.43	791.81	20.04
	10-3	149.35	228.7	709.27	789.73	21.16
16mm	16-1	235.04	230.6	707.84	786.92	23.52
	16-2	233.84	254.2	711.77	792.65	21.27
	16-3	230.70	242.2	713.46	795.45	20.27
	Average		234.7	711.49	791.74	20.48
	Deviation from standard value/%		/	-3.02	-2.75	/

2.2. Tensile test of welded joint plate

In order to analyze and study the stress mechanism of beam-column joints in high-strength steel structures, the beam-column joints were simplified with reference to European specification EC3-2015[16]. Two opposite tension plates (representing the flange of beam-column respectively) and an intermediate plate were designed and manufactured, and welded to form a "welded joint plate", as shown in the Fig.2. The uniaxial tensile test was carried out, and the test results were compared with the finite element results to verify the feasibility of the nonlinear modeling method of welded joint plate contact of high strength steel.

The real size was used for modeling in numerical simulation. After setting the constitutive relationship between Q690 high-strength steel and E76 welding rod, three contact pairs were set according to the principle of "surface-to-surface contact", namely, beam and weld, column and weld, weld and intermediate plate. After the constraint was applied at the bottom of the web, concentrated force was applied at the coupling point of its beam flange. The eight-node hexahedral linear reduced integral elements was used for division and simulation. The experimental phenomena and simulation results are shown in the Fig.3.

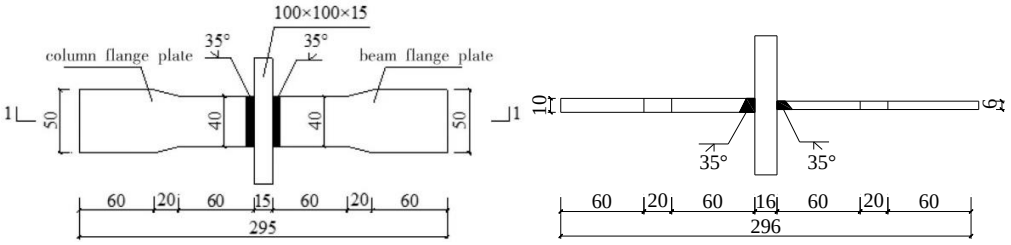

(a) Design drawing of welded joint plate specimen

(b) Welded joint plate specimen

Fig. 2 Welded joint plate

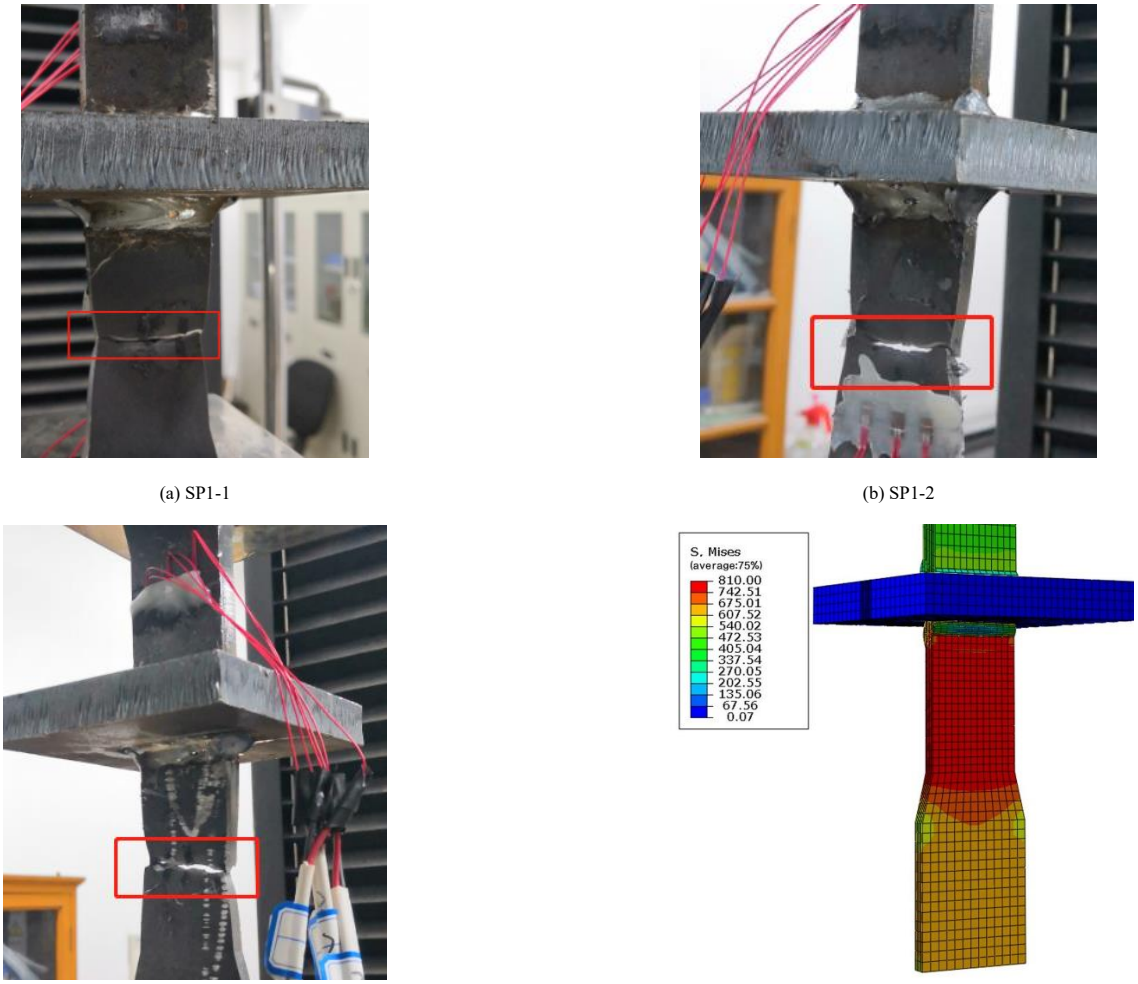

(a) SP1-1 (b) SP1-2

(c) SP1-3 (d) Finite element results

Fig. 3 Comparison of finite element simulation and experimental deformation of specimens under uniaxial tension

When the concentrated force reached 140kN, the three specimens were in the elastic stage and there was no obvious deformation. When the load was 141.63kN, SP1-3 specimen first began to yield, and then SP1-2 specimen and SP1-1 specimen also entered the yield stage. With the increase of load, the cross-sectional area of beam flange tends to decrease, and rust falls off on one side of beam flange, indicating that the steel is about to reach the ultimate bearing capacity at this time. When the load was 168.31kN, SP1-2 specimen broke first, and then SP1-3 specimen and SP1-1 specimen broke at the beam flange about 35mm away from the weld.

As can be seen from Fig.3, the maximum stress in the finite element results also appears at the flange of the beam about 35mm away from the weld, which is roughly the same as the fracture position of the three welded gusset plates in the test, thus indicating the correctness of the finite element simulation results.

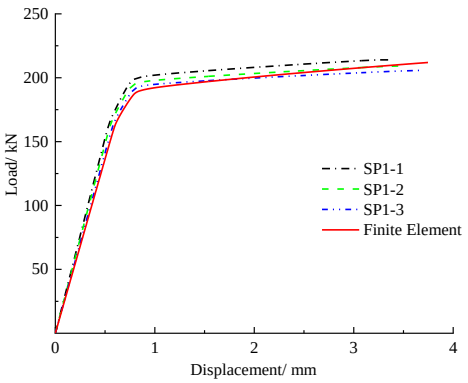

Fig. 4 Load-displacement curve of uniaxial tensile specimen

The trend of load-displacement curve obtained by test and finite element simulation is consistent and basically consistent, as shown in Fig.4. The average values of yield displacement, yield load, ultimate displacement, ultimate load, yield strength, ultimate strength and dissipated energy of the three specimens in the test are all within 5% of the simulated values.

Through the uniaxial tensile test and finite element analysis of welded joint plate specimens of high strength steel, the following conclusions are obtained:

(1) Welded joint plate specimens mostly broke at the flange of beam 35mm away from the weld under the action of uniaxial tensile test, which was similar to the failure mode simulated by finite element method.

(2) The load-displacement curves of test and simulation results under uniaxial tension are basically consistent and the error is small. The feasibility of nonlinear modeling method of welded joint plate contact of high strength steel and the effectiveness of nonlinear finite element analysis are verified, and the above finite element simulation method can continue to be used to study the mechanical properties of reinforced beam-column joints with single rib of high strength steel.

3. Design of beam-column joint specimens

In this study, models were established using Q690D steel and E76 electrode for the high-strength steel ordinary beam-column joint (ORD) and high-strength steel single-rib reinforced beam-column joint (SSR-690). Additionally, the model for the common steel single-rib reinforced beam-column joint (SSR-355) was developed using Q355B steel and J507 welding rod. Subsequently, the common steel single-rib reinforced node (SSR-355) and high-strength steel single-rib reinforced node (SSR-690) are collectively referred to as the single-rib reinforced node (SSR).

Each of the three specimens has a beam length of 1950mm, a beam section size of 300mm×150mm×8mm×13mm, a column height of 2000mm, and a column section size of 300mm×300mm×10mm×15mm. Moreover, the width-to-thickness ratios of the beams and columns comply with the Design Standards for High Strength Steel Structures [17]. The beam-column connections use a

bolt-welding combination, with all bolts being 10.9 M24 high-strength bolts [18].

In summary, the comparison of simulation results from two groups can be observed through finite element analysis: (1) Comparison between the common node and single-rib reinforced node (ORD test piece and SSR test piece); (2)Comparison between ordinary steel single-rib reinforced joints and high-strength steel single-rib reinforced joints (SSR-355 specimens and SSR-690 specimens).

According to the parameter value suggestions of the rib plate given in the US specification FEMA-350 [19] and literature [20], the parameter value of the pseudo-rib plate is $a=210\text{mm}$, $b=120\text{mm}$, $t_s=19.5\text{mm}$, $a'=40\text{mm}$, $b'=25\text{mm}$ as shown in Fig.5.

Fig.6 is a schematic diagram of two T-shaped nodes, sample numbers are shown in Table 2.

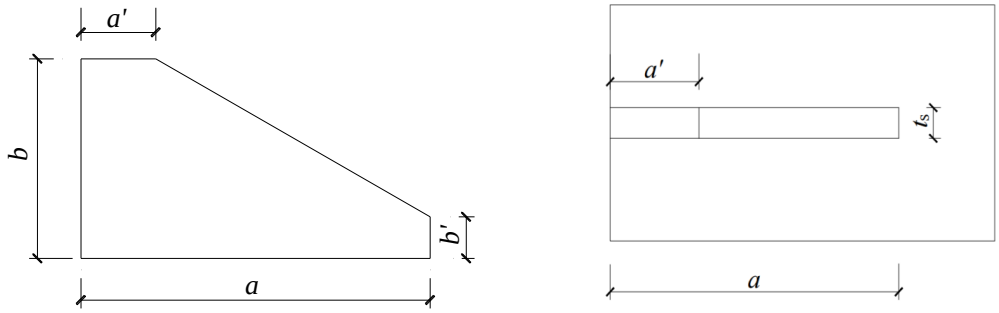

(a) Side view of floor size (b) Top view of floor dimensions

Fig. 5 Dimensional design of the rib

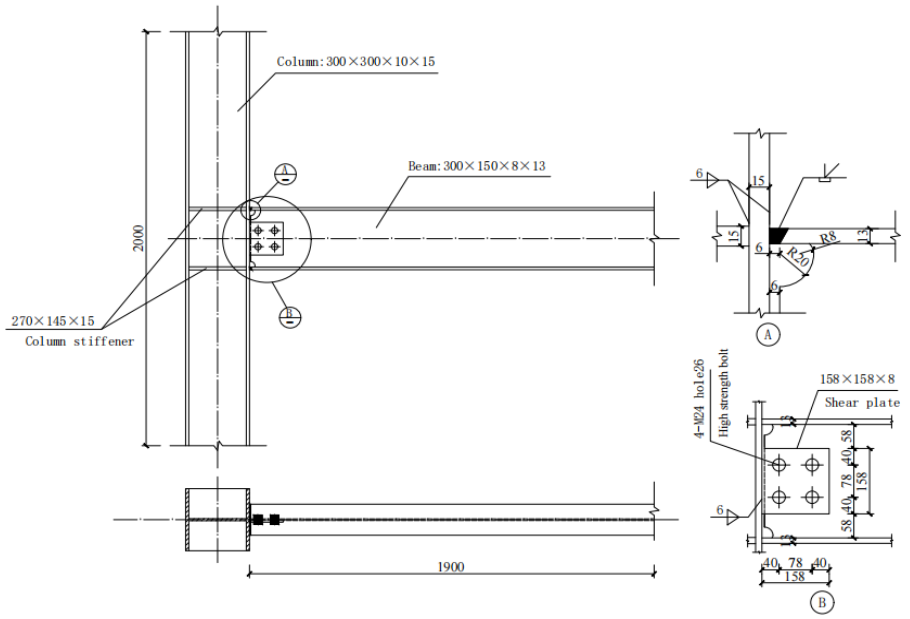

(a) High-strength steel common type joint (ORD specimen)

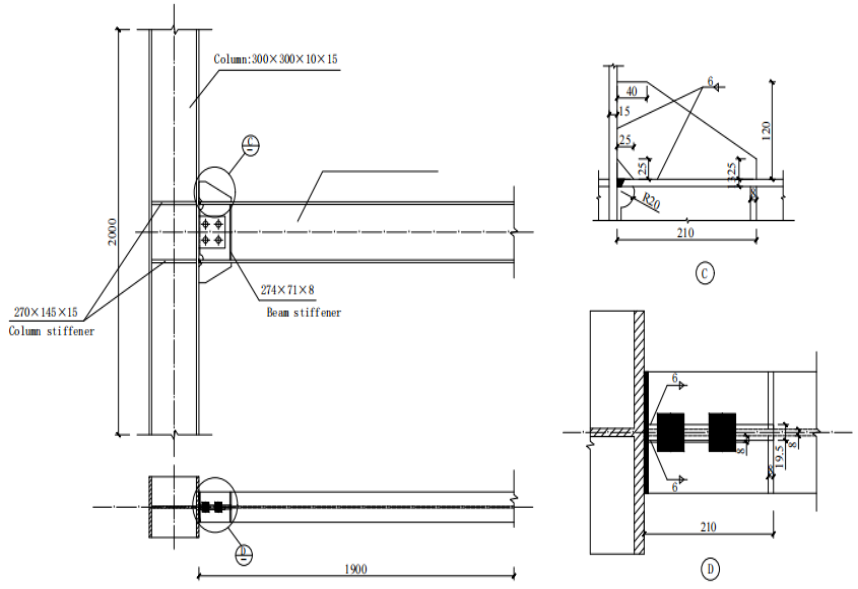

(b) Single rib reinforced joint (SSR specimen)

Fig. 6 Schematic diagram of two T-shaped nodes (unit: mm)

Table 2
Specimen number

Model	Specimen number	Beam section size/mm	Column section size/mm	Rib parameters/mm				
				a	*b*	*a′*	*b′*	t_s
ORD	ORD	300×150×8×13 (Q690D)	300×300×10×15 (Q690D)	/	/	/	/	/
SSR	SSR-355	300×150×8×13 (Q355B)	300×300×10×15 (Q355B)	210	120	40	25	19.5
	SSR-690	300×150×8×13 (Q690D)	300×300×10×15 (Q690D)	210	120	40	25	19.5

4. 3D fine finite element analysis model

4.1. Finite element modeling

All components of the model are discretized into eight-node hexahedral linear reduced integral elements (C3D8R). During the meshing process, an initial global seed layout is implemented with a unit size of approximately 30mm. Following the global distribution, the grid is further refined in key research areas. Specifically, the beam's strengthening end is extended outward by 150mm, the column's strengthening end by 100mm, and the single-rib plate is set to 10mm. The nodal domain area is established as 20mm, the weld as 1mm, and the bolt as 5mm. Additionally, intersections of the column, beam, and single-rib plate are subdivided accordingly.

In non-critical regions, the mesh is diluted, set at intervals of 100mm from 630mm above the column base to 1040mm from the loading end of the beam, as illustrated in Fig.7.

Q690D steel and E76 welding rod were used to establish finite element models for high strength steel ordinary beam-column joint (ORD) and high strength steel single rib reinforced beam-column joint (SSR-690). The material is anisotropic, the density is 7850kg/m^3, the elastic modulus is E_{Q690D}=234.7GPa, and the weld performance is selected according to [1], E_{E76}=206GPa, Poisson's ratio v=0.3. The constitutive relation of Q690D high strength steel and E76 electrode is shown in Fig.8.

Q355B steel and J507 welding rod were used to establish the finite element model of common steel single rib reinforced beam-column joint (SSR-355). Material performance parameters are selected according to [21]. The actual dimensions of all bolts refer to "Large Hexagon Bolts with High Strength for Steel Structures" (GB/T 1228-2006) [22] and are converted into cylindrical shapes and the influence of threads is ignored. 10.9 M24 high strength bolts are selected, and the performance parameters are selected according to [23]. The constitutive relations of Q355B steel and J507 electrode are shown in Fig.9, and the constitutive models of high-strength bolts are shown in Fig.10.

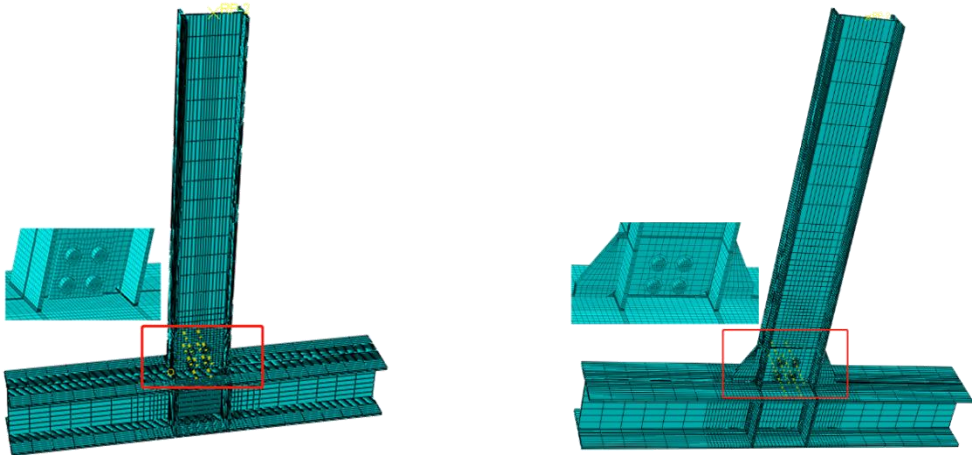

(a) ORD (b) SSR-355, SSR-690

Fig. 7 Schematic diagram of mesh division

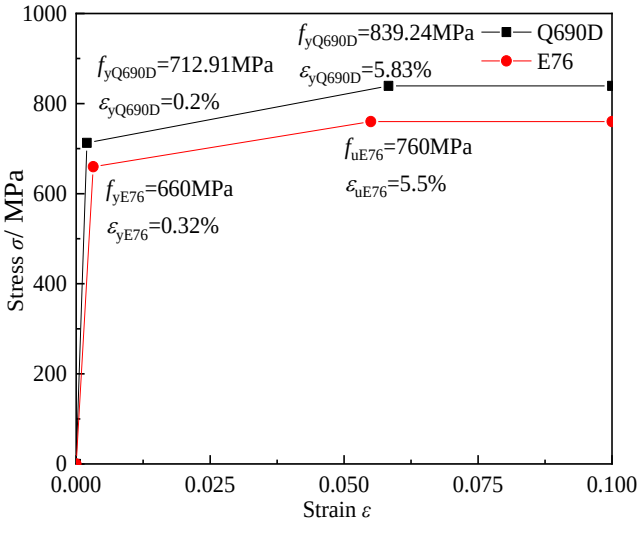

Fig. 8 Constitutive model of Q690D high strength steel and E76 weld

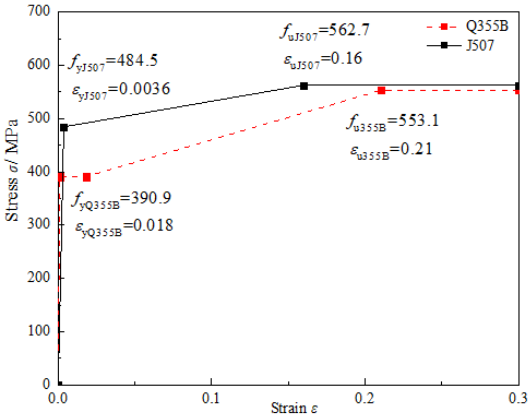

Fig. 9 Constitutive model of Q 355B steel and J507 weld

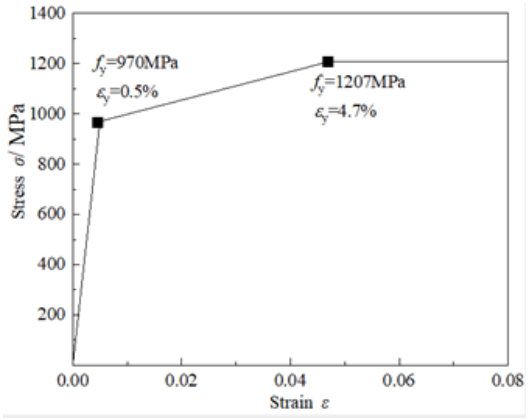

Fig. 10 Bolt constitutive model

4.2. Contact relationship

The components, such as beams, columns, shear plates, bolts, and stiffeners, are assembled into a unified structure, with constraints and contact functions established between the various entities in the interaction module. The reference point RP-2 is coupled to the beam ends through the coupling constraint command.

The binding constraints (ties) in this model include: butt weld connections between plates (between beam flanges and column flanges, horizontal stiffeners in the node domain and column webs, and between column flanges, shear plates, and column flanges), as well as fillet weld connections (between beam flanges and single rib plate, and between column flanges and single rib plate).

Additionally, numerous contact conditions are accounted for in this model, such as plate-to-plate contact (shear plate to beam web contact), plate-to-bolt contact (including contact between shear plate or beam web and bolt head or nut, and contact between the hole wall of the bolt hole and the bolt rod). The friction coefficient in this model is set to 0.5 [17].

The contact interactions in the model are summarized in Table 3, and the component interactions are illustrated in Fig.11.

Table 3
Node Model Contacts

Contact surfaces	Normal	Tangential	Friction coefficient	Quantity	Main side	From side
Shear plate - beam web	hard contact	sliding friction	0.5	1	beam web	Shear plate
Nut-Plate	hard contact	sliding friction	0.5	4	nut	plate
Bolt Head - Plate	hard contact	sliding friction	0.5	4	bolt head	plate
Screw - hole wall	hard contact	/	/	4	screw	hole wall

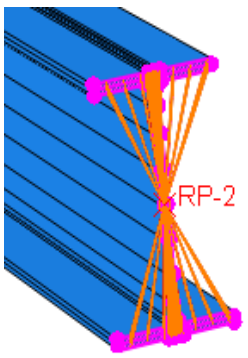

(a) Reference point coupled to beam end section

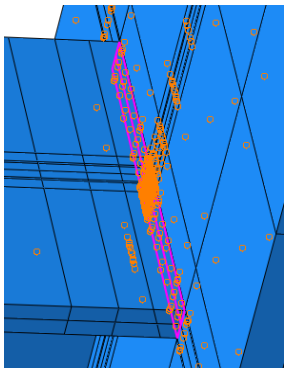

(b) Beam and column binding

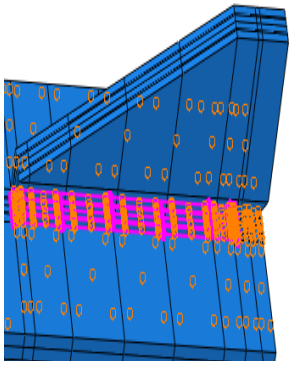

(c) Binding of single rib to beam

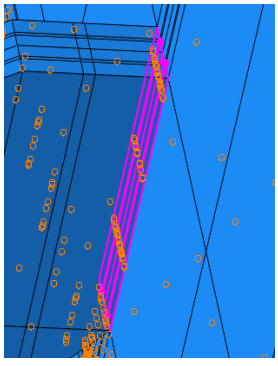

(d) Binding of single rib to column

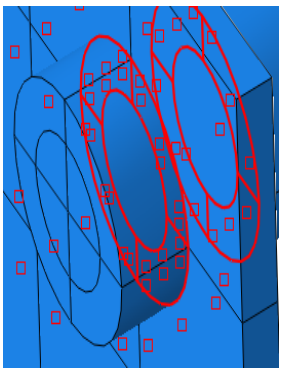

(e) Nut/bolt head in contact with plate surface

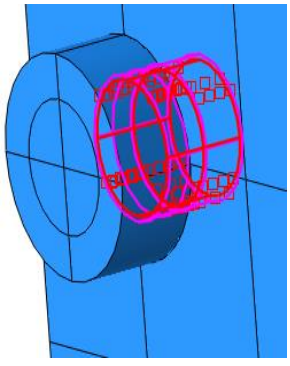

(f) The screw is in contact with the hole wall

Fig. 11 Interaction between components

4.3. Boundary conditions and loading

Based on the specifics of the actual project, the boundary constraints and loads are applied to the specimen, with reference point RP-2 coupled to the beam end through the coupling command.

In the initial analysis step (initial), full fixation is applied to the column top, column bottom, and beam end with U1=U2=U3=UR1=UR2=UR3=0.

For the Step-1 analysis, a pre-tightening force P=225kN is applied to the grade 10.9 M24 high-strength bolt using the "bolt load" command.

Moving to the Step-2 analysis, the method is changed to "fix at current length". Moreover, in this same Step-2 analysis, the "displacement/rotation" command is used to apply displacement along the positive and negative directions of the Z-axis to the reference point of the beam end via the loading system. Consequently, the boundary condition of the beam end is set as U1=UR2=UR3=0.

The model with the applied boundary conditions and loads is depicted in Fig.12.

The loading system refers to the conversion of inter-layer displacement Angle into beam end displacement recommended by ASIC[24], and the model is loaded by beam end displacement. The corresponding parameters are shown in Table 4, and the loading system is shown in Fig.13.

Table 4
Loading grading table

load level	Displacement amplitude/mm	Interlayer displacement angle/rad	Cycles
1	7.313	0.00375	6
2	9.5	0.005	6
3	14.25	0.0075	6
4	19.5	0.01	4
5	29.25	0.015	2
6	39	0.02	2
7	58.5	0.03	2
8	78	0.04	2
9	97.5	0.05	2
10	107.25	0.055	2
11	117	0.06	2

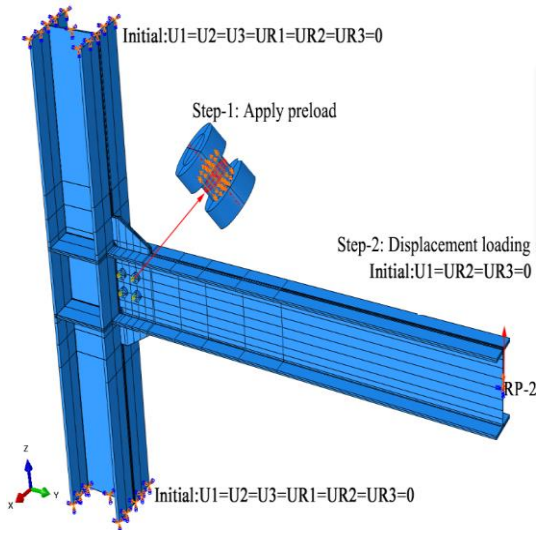

Fig. 12 Schematic diagram of boundary conditions and loading

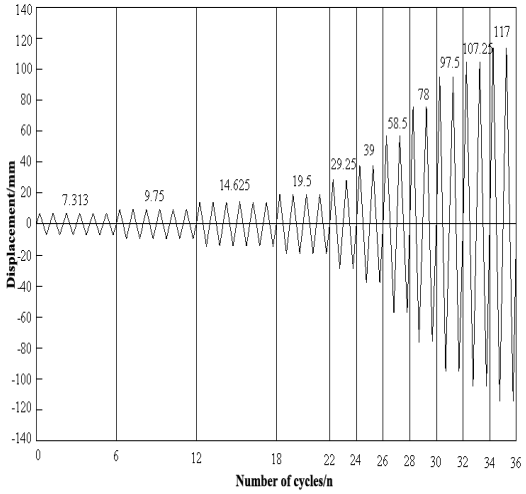

Fig. 13 Loading system

5. Analysis of hysteresis performance results

5.1. Stress cloud and failure pattern

5.1.1. ORD specimen

Fig. 14(a) illustrates that the ORD specimen is in the elastic stage during the fourth loading stage, with notable stress concentrations observed in the joint domain area, bolt, beam flange, and weld seam. Moving to Fig. 14(b), we observe that by the fifth loading stage, the specimen has entered the yield stage. Stress begins to increase in the joint domain, weld, and beam flange, predominantly concentrated in the weld and 45mm away from the column flange in the beam flange. Notably, the stress variations in the beam web, column web, and column horizontal stiffener are less pronounced during both the elastic and plastic stages.

In Fig. 14(c), as loading progresses to the seventh stage, significant stress increases are observed in the joint domain, weld, and beam flange as the specimen reaches its ultimate bearing capacity. Stress on the beam is concentrated primarily in the region 65mm away from the column flange, with stress diffusing from the beam flange to the beam web and column. Concurrently, substantial changes in stress are noted in the beam web, column web, and column horizontal stiffening rib.

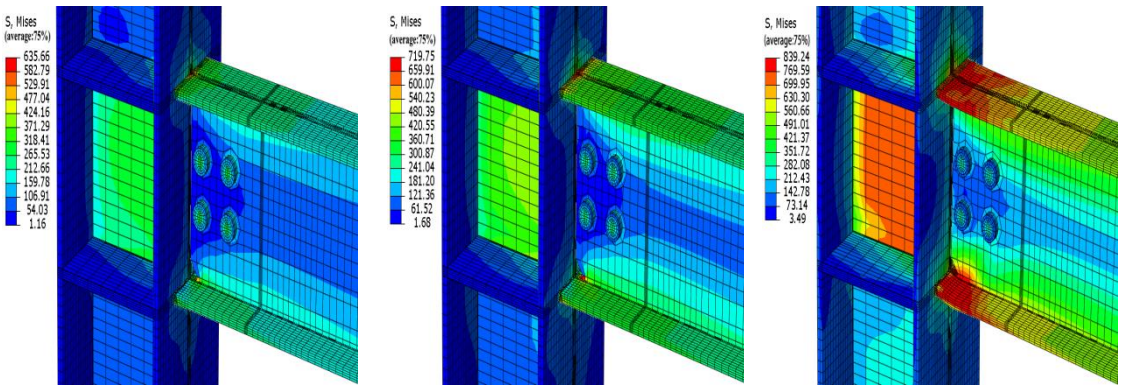

(a) Elastic stage (b) Yield stage (c) Ultimate load

Fig. 14 Stress cloud diagram of ORD specimen

5.1.2. SSR-355 specimen

In Fig. 15(a), it is evident that during the elastic stage of the SSR-355 specimen, significant stress concentrations were observed in the flange, bolt, single rib plate, and node domain, with the largest stress occurring at the bottom of the single rib plate. As the specimen transitioned into the yield stage, stress in the joint domain area, beam flange, and single rib plate began to increase. Stress then evenly diffused from the stiffening end of the rib plate to the column flange. Notable stress variations were observed in the column web and beam web, while the stress changes in the column horizontal stiffening rib were less pronounced, as depicted in Fig. 15(b).

Upon reaching the ninth loading stage, the specimen approached its ultimate bearing capacity. Consequently, stress in the joint domain area increased, and both flanges began to buckle. With continued loading and displacement, the buckling of the flange outside the stiffened end became increasingly apparent, leading to significant stress changes in each component. This highlights the node's effective utilization of the energy dissipation capacity of each component, thereby enhancing the seismic performance of the node, as illustrated in Fig. 15(c).

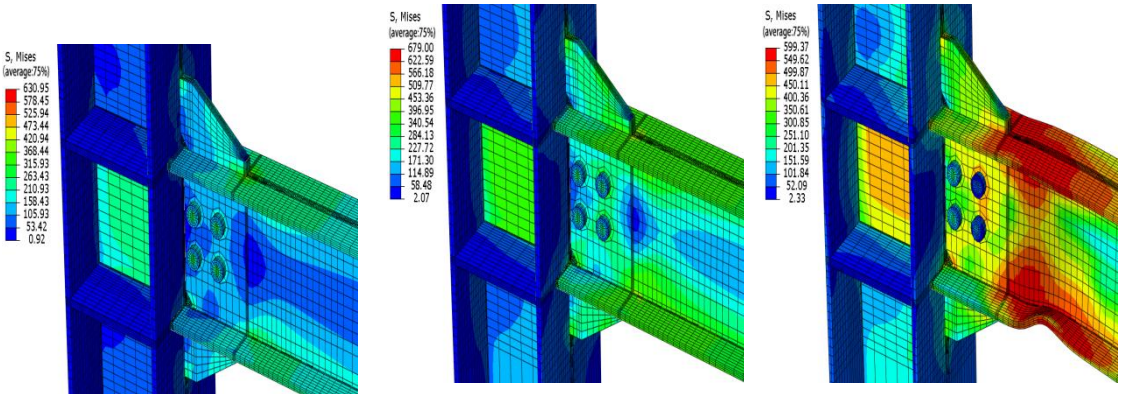

(a) Elastic stage (b) Yield stage (c) Ultimate load

Fig. 15 Stress cloud diagram of SSR-355 specimen

5.1.3. SSR -690 specimen

As depicted in Fig. 16(a), the SSR-690 specimen remained in the elastic stage during the fourth loading stage, with significant stress concentrations observed in the node domain, bolt, beam flange, and single rib plate. The maximum stress was noted at the bottom of the single rib plate end, while the stress at the weld was relatively minimal. Upon loading to the fifth stage, the specimen transitioned into the yield stage, resulting in increasing stress in the joint domain area, beam flange, and single rib plate. Stress uniformly diffused from the strengthening end to the column flange, as illustrated in Fig. 16(b). The stress variations of the web and horizontal stiffener were less pronounced during the elastic and plastic stages.

Upon reaching the ninth loading stage, the specimen approached its ultimate bearing capacity. At this stage, the stress in the joint region notably increased, with the stress on the beam primarily concentrated at the plastic hinge located 150mm away from the strengthening end. Subsequently, the flanges on both sides of the beam began to buckle. As loading continued, the buckling of the flanges became increasingly apparent. At this juncture, the single-ribbed stiffened joints effectively transferred the beam end load to the column flanges. The flanges, in turn, transmitted the force to the web and horizontal stiffeners, fully utilizing the energy dissipation capacity of each component. This enhanced the seismic performance of the joint, as illustrated in Fig. 16(c).

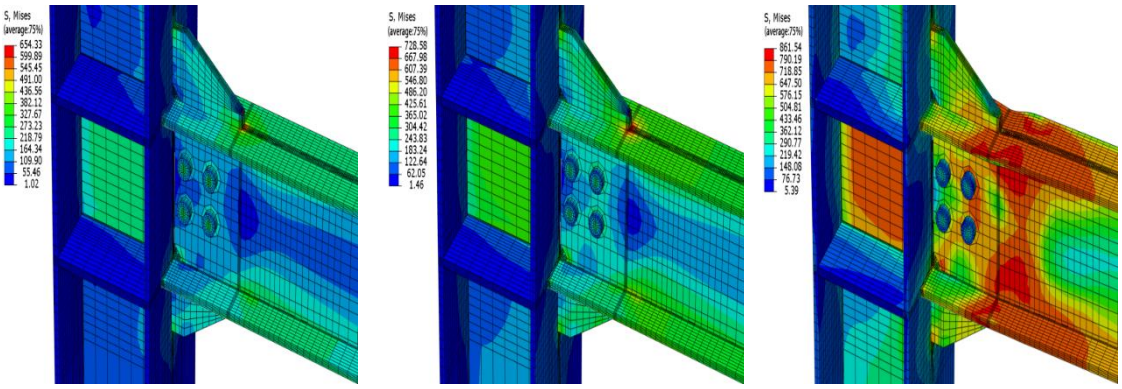

(a) Elastic stage (b) Yield stage (c) Ultimate load

Fig. 16 Stress cloud diagram of SSR-690 specimen

By conducting a comparative analysis of stress distribution maps and failure modes among the three specimens, several conclusions can be drawn. The ORD specimens primarily exhibited significant stress concentrations and damage at the weld and the flange approximately 65mm away from the weld. In contrast to the ordinary joints, the SSR-355 and SSR-690 specimens displayed less noticeable deformation in the weld and heat-affected zone throughout the entire loading process. Damage in these specimens predominantly occurred at the plastic hinge, showcasing a better protection mechanism for the beam-column connection against damage.

From the above numerical results, we can observe that there are significant differences in the failure locations between the ORD specimen and the SSR specimen.

In the ORD specimen, the weld is a critical area. The weld may have inherent defects which can act as stress-raisers and reduce the overall strength of the welded joint. Additionally, the material properties of the weld may not be as favorable as the base material in terms of strength and ductility. The combination of stress concentration and the relatively lower strength of the weld material makes it the most vulnerable location for failure in the ORD specimen.

The SSR specimen, with its single-rib reinforcement, changes the stress distribution pattern. The rib acts as an additional structural element that helps to reduce the stress concentration at the weld area and shifts the stress to other regions. As the load is applied to the SSR specimen, the stress is concentrated in the area where the plastic hinge forms. Eventually, as the plastic deformation accumulates and the material reaches its ultimate deformation capacity, the plastic hinge fails, leading to the overall failure of the SSR specimen.

In summary, the ORD specimen fails at the weld due to the combination of welding-related weaknesses and stress concentration at the weld joint. In contrast, the SSR specimen's single-rib reinforcement changes the stress distribution, leading to the formation and failure of a plastic hinge as the critical failure mode. This difference in failure locations highlights the impact of reinforcement on the structural behavior and failure mechanisms of the specimens.

5.2. Hysteresis curve

Figs. 17(a)-(c) reveal that the hysteresis curves of ORD specimens appear elongated and flat, whereas those of SSR-355 and SSR-690 specimens exhibit a more fusiform and complete shape. The area under the hysteretic curve for SSR-355 and SSR-690 specimens is notably larger compared to that of ORD specimens. This observation suggests that the single rib plate reinforced joints formed plastic hinges outside the strengthened end, thereby enhancing the dissipation of seismic energy and mitigating the risk of brittle failure in the butt weld. Furthermore, as depicted in Fig. 17(d), the ultimate bearing capacity of the SSR-690 specimen surpasses that of the ORD and SSR-355 specimens significantly, indicating the highest bearing capacity among high-strength steel single-rib reinforced joints [25].

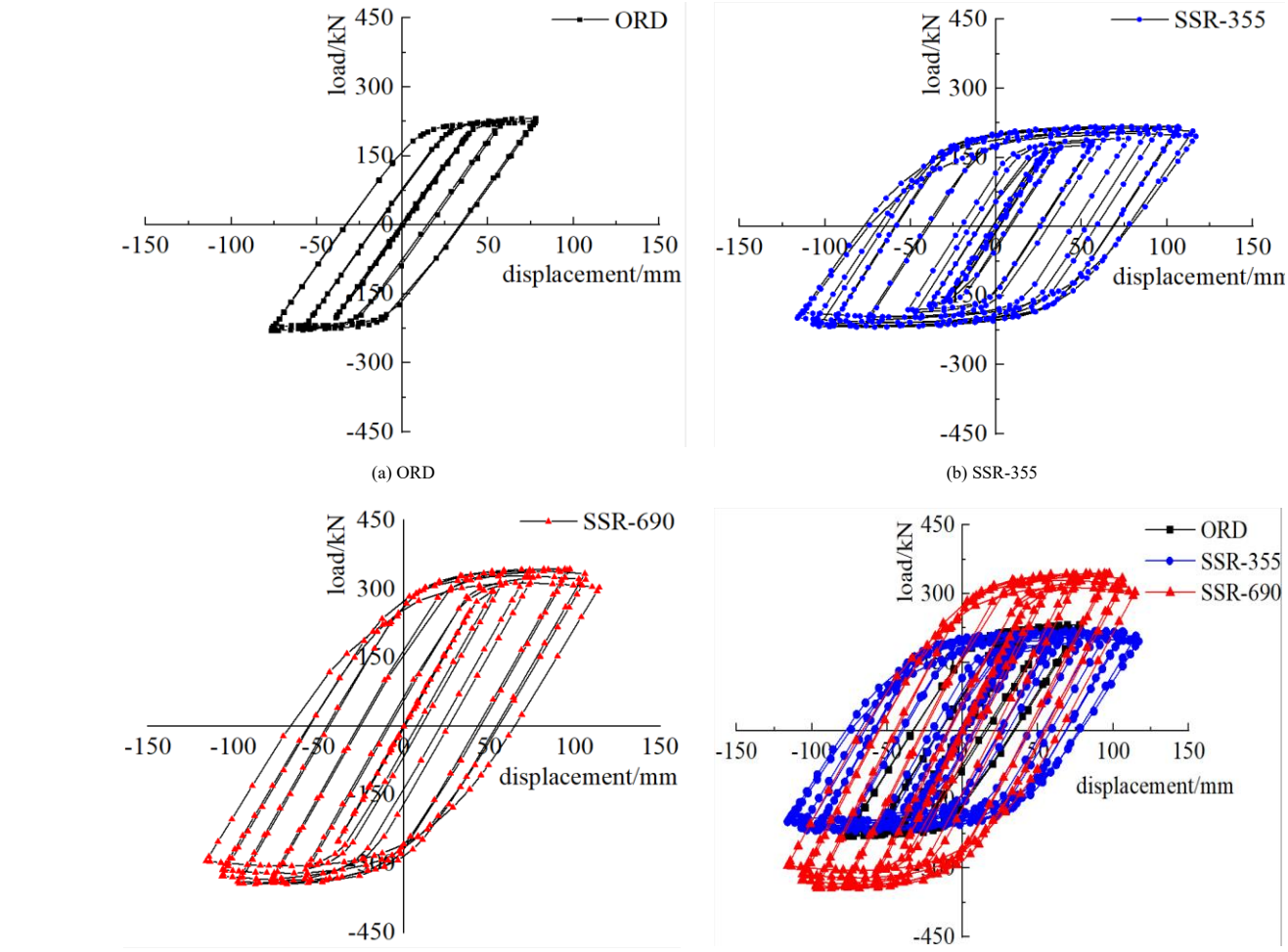

(a) ORD (b) SSR-355

(c) SSR-690 (d) Comparison of hysteresis curves

Fig. 17 Hysteresis curve

5.3. Skeleton Curve

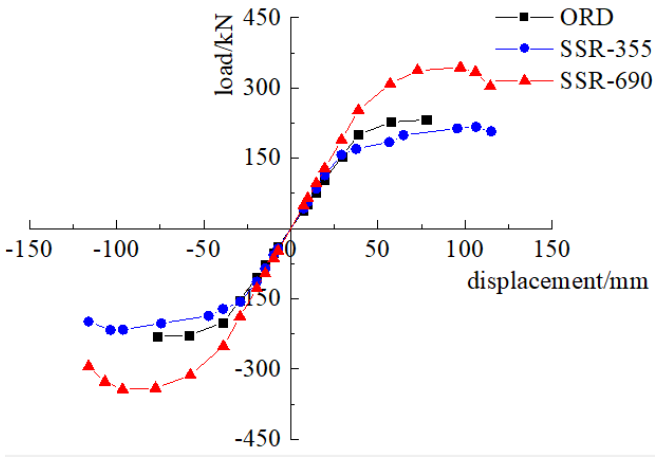

Fig. 18 Skeleton curve

As illustrated in Fig. 18, all three specimens exhibited elastic, yield, and failure stages, indicating the occurrence of plastic deformation in each type of joint. Upon reaching the fourth loading stage, both the ORD specimen and SSR specimen remained in the elastic stage, with the load increasing proportionally to the displacement. Subsequently, when loaded to the fifth stage, all three specimens exhibited a turning point and entered the yield stage. Notably, the ORD specimen reached its ultimate bearing capacity by the seventh loading stage, whereas the SSR specimen achieved its ultimate bearing capacity stage only by the ninth stage, experiencing three additional loading stages compared to the ORD specimen. Throughout each loading stage, the skeleton curve of the SSR-690 specimen consistently enveloped that of the SSR-355 specimen and ORD specimen, underscoring the high bearing capacity of high-strength steel single-rib reinforced joints [26].

5.4. Bearing capacity and ductility properties

Upon reviewing the statistical data presented in Table 5, it becomes apparent that the forward ultimate load of both the ORD and SSR specimens exceeds the negative ultimate load, thus establishing the forward ultimate load as the specimen's ultimate bearing capacity. A comparative analysis reveals that the yield load of the SSR-355 and SSR-690 specimens increased by 2.88% and 23.34%, respectively, in comparison to the ORD specimens. Furthermore, the ultimate displacement exhibited a notable increase of 49.92% and 46.91% for the SSR-355 and SSR-690 specimens, respectively. Particularly, the ultimate load of the SSR-690 specimens showcased a significant surge of 48.16%. Conversely, the ultimate load of the SSR-355 specimen was 6.48% lower than that of the ORD specimen, suggesting that the reinforced single-rib joint enhances the node's deformation capacity, while the node's ultimate bearing capacity can be further enhanced by augmenting the yield strength [27].

In comparison to the SSR-355 specimens, the SSR-690 specimens displayed an increased yield load of 19.89% and an escalated ultimate load of

58.42%. However, there was a marginal decrease of 2.01% in the ultimate displacement. This indicates that high-strength steel single-rib reinforced joints offer an enhancement in the ultimate bearing capacity of joints, albeit with a slight reduction in deformation.

Table 5
Displacement load and ductility coefficient

Specimen	Force direction	Yield displacement (mm)	yield load (kN)	limit displacement (mm)	ultimate load (kN)	Ductility coefficient μ
ORD	just	29.15	152.98	77.97	232.01	2.67
	burden	- 29.13	- 150.64	- 76.83	- 229.82	2.64
SSR-355	just	29.12	157.38	116.90	216.99	4.01
	burden	- 29.01	- 156.42	- 116.11	- 216.81	4.00
SSR-690	just	29.16	188.68	114.54	343.75	3.93
	burden	- 29.21	- 189.39	- 116.05	-343.24	3.97

As indicated in Table 5, the ductility coefficients of ORD specimens, in both positive and negative directions, fall below 3.0. Conversely, the ductility coefficients of SSR-355 and SSR-690 specimens, in both positive and negative directions, exceed 3.0, underscoring the inadequate ductility of ordinary joints and the favorable ductility exhibited by the single-rib reinforced joints. Notably, the ductility coefficients of SSR-355 and SSR-690 specimens surpassed those of ORD specimens by 50.19% and 47.19%, respectively, demonstrating that the reinforced single rib plate facilitates the optimal utilization of joint ductility and ensures its effectiveness. Moreover, the ductility coefficient of SSR-690 specimens exhibited a marginal 2.00% decrease compared to that of SSR-355 specimens, indicating a potential decrease in joint ductility with an increase in yield strength.

5.5. Stiffness degradation

Fig. 19 illustrates the stiffness degradation curves of the three specimens. Upon comparison of these curves, it becomes apparent that, when subjected to the same displacement loading amplitude, the SSR-355 specimen exhibits a notably faster stiffness degradation rate in contrast to the ORD specimen and SSR-690 specimen. This observation suggests that an elevation in the yield strength of steel has the potential to defer the stiffness degradation rate of joints. Moreover, the stiffness degradation rate of the ORD specimen significantly outpaces that of the SSR-690 specimen. This finding underscores that, for high-strength steel beam-column joints, the displacement of the plastic hinge towards the outer regions via a single rib plate can enhance the joint stiffness and delay its degradation, thereby augmenting its seismic resilience.

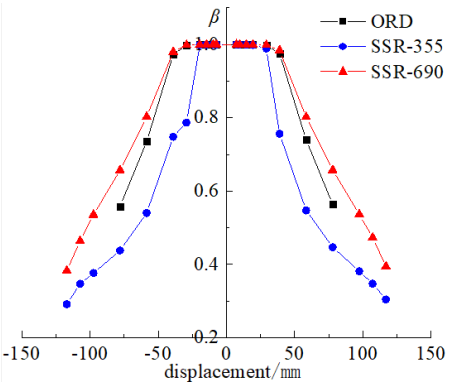

Fig. 19 Comparison of stiffness degradation curves

Based on the above analysis, in comparison with the ORD and SSR-355 joints, the SSR-690 joint exhibits a slower rate of stiffness degradation. Primarily, this is attributable to the fact that the Q690D steel possesses a relatively high yield strength and favorable ductility. Moreover, the geometric configuration of the joint also exerts a non-negligible influence. In contrast to other joints, the single rib plate incorporated in the SSR-690 specimen is capable of augmenting the moment of inertia and section modulus of the joint. This, in turn, facilitates a more efficient distribution of internal forces and mitigates the local stress peaks, thereby contributing to the deceleration of the joint's stiffness degradation. The combination of high-strength materials and the optimized geometric shape endows the SSR-690 joint with enhanced capacity to resist the applied loads.

5.6. Energy consumption capacity

In this study, the equivalent viscous damping coefficient h_e was calculated by energy dissipation coefficient E_h [28]. The energy dissipation calculation diagram is shown in Fig.20. The hysteresis loop in the figure is the last complete hysteresis loop in the load-displacement curve. The calculation formula is as follows:

$$E_h = \frac{S_{ABCD}}{S_{OAE} + S_{OCF}} \tag{1}$$

$$h_e = \frac{1}{2\pi} \cdot E_h \tag{2}$$

where S_{ABCD} is the shaded area in Fig.20, S_{OAE}, S_{OCF} are the areas of triangle OAE and triangle OCF in Fig.20.

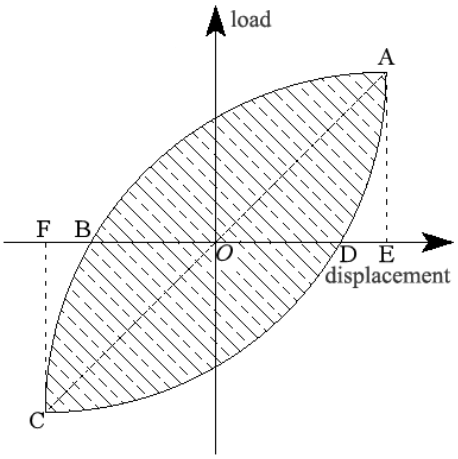

Fig. 20 Calculation diagram of energy dissipation coefficient

Compared with the data in the table, The S_{ABCD} of SSR-355 and SSR-690 specimens increased by 48.52% and 116.41%, respectively, compared with ORD specimens. The sum of the areas of S_{OAE} and S_{OCF} increased by 26.63% and 97.97%, E_h by 17.36% and 9.43%, h_e by 17.30% and 9.48%, respectively. The reason is that all the energy of ORD specimen is absorbed by the weld between the beam and column, while the single rib plate of SSR specimen flexes and absorbs the energy, thus achieving the function of energy dissipation and node protection. It indicates that the reinforced single rib joints have better energy dissipation capacity [29]. Compared with SSR-355, the sum of areas of S_{ABCD}, S_{OAE} and S_{OCF} of SSR-690 specimens increased by 45.71% and 56.34% respectively, while h_e decreased by 6.67%, indicating that energy dissipation capacity decreased slightly with the increase of yield strength.

Table 6
Equivalent Viscous Damping Coefficient h_e

Specimen	S_{ABCD}	$S_{OAE}+S_{OCF}$	E_h	h_e
ORD	46117.27	17383.81	2.65	0.422
SSR-355	68494.32	22013.03	3.11	0.495
SSR-690	99804.17	34415.23	2.90	0.462

6. Conclusions

In this study, ABAQUS finite element analysis was conducted on high-strength steel common joints (ORD specimen), common steel single-rib reinforced joints (SSR-355 specimen), and high-strength steel single-rib reinforced joints (SSR-690 specimen). The study comprehensively investigated the failure modes, hysteretic curves, ductility, load-bearing capacity, stiffness degradation, energy dissipation capacity, and other hysteretic properties of these joints. The following conclusions were drawn from the analysis:

(1) The ORD specimen exhibited severe damage and destruction in the weld and varying degrees of damage in the heat-affected zone. In contrast, SSR-355 and SSR-690 specimens achieved the objective of outward plastic hinge movement through a single rib plate. This resulted in relatively minor deformation at the weld, thereby safeguarding the beam-column butt weld, ultimately leading to buckling failure at the plastic hinge position.

(2) The hysteretic performance indices of SSR specimens demonstrate significant advantages, with the hysteretic area of SSR specimens notably exceeding that of ORD specimens. When compared with ORD specimens, the yield load of SSR-355 and SSR-690 specimens increased by 2.88% and 23.34%, respectively, and the ultimate displacement increased by 49.92% and 46.91%, respectively. Furthermore, the ultimate load of SSR-690 specimens increased by 48.16% compared to ORD specimens.

However, in comparison with ORD specimens, the ultimate load of SSR-355 specimens decreased by 6.48%. Nonetheless, the ductility coefficient increased by 50.19% and 47.19% for SSR-355 and SSR-690 specimens, respectively. Moreover, the initial stiffness increased by 10.42% and 24.62%, and the equivalent viscous damping coefficient he increased by 17.30% and 9.48% for SSR-355 and SSR-690 specimens, respectively. These findings indicate that the single-rib plate stiffened joint can enhance the deformation capacity and initial stiffness of the joint, while also exhibiting improved ductility and energy dissipation capacity.

(3) In comparison with SSR-355 specimens, SSR-690 specimens exhibited an increase of 19.89%, 58.42%, and 12.85% in yield load, ultimate load, and initial stiffness, respectively. The secant stiffness values of SSR-690 specimens surpassed those of SSR-355 specimens. However, there was a decrease of 2.01%, 2.00%, and 6.67% in ultimate displacement, ductility coefficient, and ductility coefficient, respectively. These results indicate that enhancing the steel strength can elevate joint stiffness and decelerate the stiffness degradation rate. However, it also leads to a reduction in energy dissipation capacity and ductility as the yield strength increases.

Acknowledgments

The authors are grateful for the supports of the Opening Fund of State Key Laboratory of Green Building in Western China (No.LSKF202324), and Yangzhou Government-Yangzhou University Cooperative Platform Project for Science and Technology Innovation(No.YZZP202206), and Postgraduate Research & Practice Innovation Program of Jiangsu Province (Yangzhou University) (No.SJCX23_1944).

References

[1] Hu F, Wang Z. Cyclic Behavior of Dual-Steel Beam-to-Column Welded Flange-Bolted Web Connections[J]. Thin-Walled Structures,2024.
[2] Jiang S , Shi G , Zhang N ,et al.Experimental study on seismic behavior of cover-plate connections between steel beams and high strength steel box columns[J].Thin-Walled Structures, 2023, 193.
[3] Jiang J ,Bao W ,Yu Y , et al.Experimental study on crack propagation characteristics of welded high-strength steel Q690CFD joints[J].Journal of Constructional Steel Research,2025,225:109177
[4] ZHENG Hao. Hysteretic performance and parametric analysis of steel frame beam-column joints with replaceable extended-wing T-joints [D]. Jiangsu: Yangzhou University, 2020.
[5] WANG Yan. Seismic Design Theory and application of New Ductile Joints in steel Structure [M]. Beijing: Science Press, 2012.
[6] Ma H.W., Zheng H., Zhang W., et al. Experimental and numerical study of mechanical properties for the double-ribbed reinforced beam-column connection[J]. Advanced Steel Construction, 2020, 4(16): 297-309.
[7] Liang Z ,Shi-Chao G ,Heng L , et al. Experimental and numerical investigation on fatigue behaviors of Q690D butt welds[J].Journal of Constructional Steel Research,2023,211
[8] Shuai L ,Zhiqiang W ,Huan L , et al. Optimization of welding parameters on welding distortion and stress in S690 high-strength steel thin-plate structures[J].Journal of Materials Research and Technology,2023,25382-397.
[9] Jordao S., Da S. L. S., Simoes R. Design formulation analysis for high strength steel welded beam-to-column connections[J]. Engineering Structures, 2014, 70: 63-81.
[10] Guo H ,Zheng D ,Zhang J , et al. Experimental study on the seismic performance of angle connected high-strength steel moment resisting beam-column joint[J].Journal of Constructional Steel Research,2024,222108940-108940.
[11] Hongchao G ,Xizhe Z ,Wei L, et al. Experimental and numerical study on seismic performance of Q690 high-strength steel plate reinforced joints[J].Thin-Walled Structures,2021,161
[12] Lu Linfeng, Yan Ji, Yu Haojie. Finite element analysis on the seismic behavior of the new ribs reinforced connection for minor-axis of I-section column [J]. Steel Construction,2016,31(09):1-6.
[13] Wang Lu, Wang Wuxing, Tang Hongchun. Research on hysteretic behavior of single-rib-reinforced steel moment connections in steel frame [J]. Steel Construction,2019,34(01):7-14.
[14] Yang Tao, Wang Yan. Research on Mechanical Properties of Stiffened Joint Domain of Steel Frame Rib Plate. Steel Structure, 2015, 30(02): 1-6+44.
[15] GB/T 2975-2018. Steel and steel products -- sampling location and sample preparation for mechanical properties test [S]. Beijing: China Architecture and Architecture Press, 2018.
[16] CEN, ENV1993-1-8 Eurocode 3: Design of Steel Structures, Part 1.8: Design of connections[S]. European Committee for Standardization.2015.
[17] JGJ/T 483-2020. High strength Steel structure Design Standard [S]. Beijing: China Architecture and Architecture Press, 2020.
[18] WANG Yan. Seismic Performance Design Theory and application of New Ductile Joints in steel structure [M]. Beijing: Science Press, 2012.
[19] FEMA-350. Recommended Seismic Design Criteria for New Steel Moment-Frame Buildings[S]. Washington D. C.: Federal Emergency Management Agency, 2000
[20] ZHAO Ying. Analysis of hysteretic behavior and fracture behavior of beam-column joints with symmetric double-ribbed reinforced steel frames [D]. Jiangsu: Yangzhou University, 2019.
[21] Zhang W. Y., Zeng L. J. Experimental investigation and low-cycle fatigue life prediction of welded Q355B steel[J]. Journal of Constructional Steel Research, 2021, 178: 106497.
[22] GB/T 1228-2006. High strength bolts with large hexagon head for steel structure [S]. Beijing: China Planning Press, 2006.
[23] Qi Jingxuan. Study on seismic behavior of high-strength steel beam-to-column end-plate connections[D]. Shaanxi: Xi 'an University of Technology, 2017.
[24] AISC. Seismic Provisions for Structural Steel Buildings[S]. Chicago: American Institute of Steel Construction, 2016.
[25] Farooghi M. S. M. R., Ghobadi M. S. Seismic performance of retrofitted WFP connections joined to box column using ribs[J]. Journal of Constructional Steel Research, 2017, 137: 297-310.
[26] Wang K., Lu X. F., Yuan S. F., et al. Analysis on hysteretic behavior of composite frames with concrete-encased CFST columns[J]. Journal of Constructional Steel Research, 2017, 135: 176-186.
[27] Ma Hongwei, Lyu Dianmei, ZHAO Ying, et al. Seismic behavior of the symmetrical double-ribbed reinforced beam-column connections of steel frames[J]. Journal of Yangzhou University (Natural Science Edition), 2020, 23(01): 59-67.
[28] Ma Hongwei, ZHAO Ying, Wang Zijian, et al. Hysteretic behaviour analysis of new beam-column connections with expanded flange of steel frame[J]. Journal of Yangzhou University (Natural Science Edition), 2018, 21(1): 50-55.
[29] Song Q. Y., Heidarpour A., Zhao X. L., et al. Performance of flange-welded/web-bolted steel I-beam to hollow tubular column connections under seismic load[J]. Thin Wall Struct, 2017, 116: 250-264.